Research Square

Preprints are preliminary reports that have not undergone peer review.
They should not be considered conclusive, used to inform clinical practice,
or referenced by the media as validated information.

Phthalate-Induced Uterine Wall Remodeling Alters Organ-Level Biomechanics

Mahmuda Raakib Arshee
University of Illinois at Urbana-Champaign
Sophia Caron
University of Illinois at Urbana- Champaign
Mary J. Laws
University of Illinois at Urbana- Champaign
Jodi A. Flaws
University of Illinois at Urbana- Champaign
Indrani C. Bagchi
University of Illinois at Urbana- Champaign
Amy Wagoner Johnson
ajwj@illinois.edu

University of Illinois at Urbana-Champaign

Article

Keywords:

Posted Date: November 10th, 2026

DOI: https://doi.org/10.21203/rs.3.rs-11332921/v1

License: This work is licensed under a Creative Commons Attribution 4.0 International License.
Read Full License

Additional Declarations: No competing interests reported.

Phthalate-Induced Uterine Wall Remodeling Alters Organ-Level Biomechanics

Mahmuda Raakib Arshee [1], Sophia Caron [2], Mary J. Laws [2], Jodi A. Flaws [2,4], Indrani C. Bagchi [2,4.5], Amy Wagoner Johnson [1,3,4,5,6]

[1] Mechanical Science and Engineering, Grainger College of Engineering, University of Illinois at Urbana-Champaign, Urbana, IL, 61801, USA

[2] Comparative Biosciences, College of Veterinary Medicine, University of Illinois at Urbana-Champaign, Urbana, IL, 61802, USA

[3] Biomedical and Translational Sciences, Carle Illinois College of Medicine, University of Illinois at Urbana-Champaign, Champaign, IL 61820, USA

[4] Carl R. Woese Institute for Genomic Biology, University of Illinois at Urbana-Champaign, Urbana, IL, 61801, USA

[5] Biohub Chicago, LLC, Chicago, IL, 60642, USA

[6] Beckman Institute for Advanced Science and Technology, University of Illinois at Urbana-Champaign, Urbana, IL, 61801, USA

* Corresponding author at Mechanical Science and Engineering, Grainger College of Engineering, University of Illinois at Urbana-Champaign, Urbana, IL, 61801, USA
Email address: ajwj@illinois.edu

Abstract

Phthalates are endocrine-disrupting chemicals associated with adverse reproductive outcomes and uterine extracellular matrix remodeling. However, whether such remodeling alters organ-level uterine mechanics remains unknown. Uterine horns from mice exposed to a phthalate mixture (0, 0.15, 1.5, or 1500 ppm for one year) underwent balloon inflation testing to characterize mechanical behavior and second harmonic generation imaging to quantify wall geometry and collagen microstructure. Exposure reduced endometrial (Em) area, increased circumferential myometrial (CM) thickness, and decreased Em:CM area and thickness ratios, while increasing inflation stiffness, work, and resistance. Lower Em ratios correlated with greater inflation resistance. An image-informed, three-layer finite element model showed that geometric redistribution alone, with constitutive properties unchanged, reproduced experimental inflation trends, reduced deformation, and redistributed layer-specific stresses and strains. Within the investigated ranges, geometric remodeling influenced inflation mechanics more than twofold CM stiffening, identifying uterine wall geometry as a key determinant of passive biomechanics following phthalate exposure.

Introduction

Environmental toxicants have emerged as important contributors to adverse reproductive health outcomes [1–4]. Among these, phthalates are widely used plasticizers present in numerous consumer products, resulting in widespread human exposure [5–11]. As endocrine-disrupting chemicals, phthalates can interfere with hormonally regulated tissue remodeling processes, including extracellular matrix turnover and collagen microstructure [12]. Chronic phthalate exposure has been associated with infertility, impaired implantation, pregnancy complications, and altered uterine physiology, suggesting that these chemicals may compromise both the structure and function of the uterus [13–20].

The uterus is a mechanically active organ that undergoes extensive deformation throughout the reproductive lifespan, including during menstruation, implantation, pregnancy, and parturition [21–23]. Its mechanical response depends on the organization of the uterine wall, which consists of the endometrium (Em) and two anatomically distinct myometrial layers embedded within a collagen-rich extracellular matrix [24, 25]. The Em forms the inner uterine lining, while the myometrium is composed predominantly of smooth muscle cells and is organized into circumferential (CM) and longitudinal (LM) layers according to their predominant orientations. Myometrial smooth muscle generates the contractile forces required for uterine function, while the surrounding collagen-rich extracellular matrix provides passive mechanical support during deformation. The architecture of the uterine wall, including the tissue constituents composition, layer geometry, and collagen microstructure, governs the passive mechanics of the uterus during loading [26–29]. Here, uterine wall geometry refers collectively to layer thicknesses, cross-sectional areas, and relative layer proportions. Consequently, geometric remodeling of the uterine wall has the potential to alter organ-level mechanical function.

Previous studies have demonstrated that chronic phthalate exposure induces extracellular matrix remodeling, altered collagen organization, fibrotic changes, inflammatory responses, and changes in uterine morphology [16, 19, 30–33]. However, these investigations have focused primarily on molecular and histological outcomes, and whether exposure-induced remodeling translates into measurable changes in organ-level mechanics has remained largely unknown. Establishing this relationship is essential for understanding how environmental toxicants influence uterine function.

To address this gap, the first part of this study combined organ-level balloon inflation testing with quantitative characterization of uterine wall geometry. Pressure–volume measurements were used to quantify inflation mechanics, while second harmonic generation (SHG) imaging provided measurements of layer areas, thicknesses, and relative proportions. Correlation analyses were then used to evaluate relationships between uterine wall geometry and organ-level inflation mechanics and to identify geometric features for subsequent computational investigation.

Although these experimental analyses allowed relationships between uterine wall geometry and inflation mechanics to be evaluated, they could not determine whether changes in geometry directly contributed to the altered mechanical response. Chronic phthalate exposure can

simultaneously affect multiple biological processes, including extracellular matrix composition, collagen organization, and tissue material properties, making it difficult to isolate the mechanical effects of geometric remodeling through experimental measurements alone. In addition, previous nanoindentation measurements demonstrated increased stiffness of the CM following chronic phthalate exposure, indicating that changes in material properties may also contribute to the altered inflation response [12]. Thus, the independent contributions of geometric remodeling and CM stiffening to organ-level inflation mechanics remain unclear.

Finite element (FE) modeling provides a framework for addressing this limitation by allowing individual geometric and material variables to be investigated independently [34, 35]. Because the Em, CM, and LM each exhibit distinct collagen fiber microstructure, orientation, and material properties, their individual mechanical contributions can combine to determine the overall passive behavior of the uterine wall. Conventional models that represent the uterus as a homogeneous material overlook this layered anatomy, limiting their ability to capture how each compartment contributes to organ-level mechanics or how layer-specific changes, such as those induced by phthalate exposure, propagate to alter whole-organ mechanical behavior. A layered, image-informed FE model is therefore needed to resolve the individual and combined mechanical roles of each uterine wall layer.

In the present study, SHG-derived measurements were used to reconstruct an image-informed three-layer FE model of the uterine wall. The FE framework was used to independently evaluate the mechanical contributions of geometric remodeling and CM stiffening to organ-level inflation behavior and layer-specific stress and strain distributions. We hypothesized that geometric remodeling of the uterine wall, independent of CM stiffening, would be sufficient to alter organ-level inflation mechanics and layer-specific stress and strain distributions. Together, experimental and computational approaches were used to investigate how phthalate-induced geometric and material remodeling contribute to altered uterine biomechanics.

Results

Phthalate exposure remodels uterine wall geometry

Representative SHG images demonstrated differences in uterine wall geometry following chronic phthalate exposure (Fig. 1A, Supplementary Fig. S1). Compared with controls, exposed tissues exhibited a visibly smaller Em compartment and a thicker CM.

Quantitative analysis of the geometric parameters confirmed these geometric changes. Em area was significantly reduced in all phthalate-exposed groups relative to controls (Fig. 1B). Local CM thickness was significantly greater in all exposed groups compared with controls, and additional significant differences were observed between the low and high exposure groups and between the medium and high exposure groups (Fig. 1C).

Changes in the relative geometry of the Em and CM were similarly evident from the layer ratios. The Em:CM area ratio was significantly reduced in the medium and high exposure groups relative

to controls (Fig. 1D). Likewise, the Em:CM thickness ratio was significantly reduced in the medium and high exposure groups compared with controls (Fig. 1E). Additional measurements of CM area, LM area, total uterine cross-sectional area, and local Em thickness are provided in Supplementary Fig. S2.

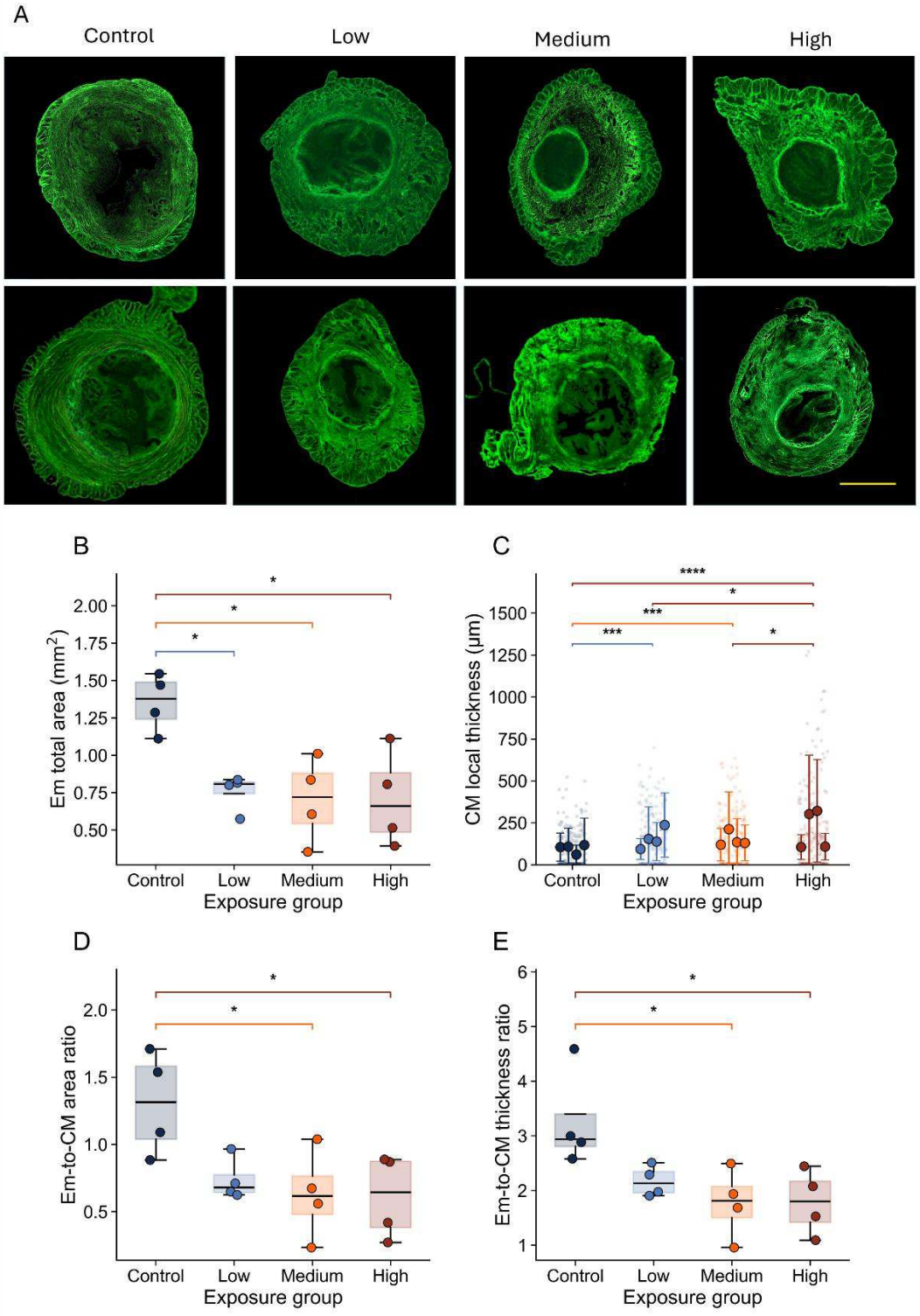


Fig. 1 Chronic phthalate exposure remodels uterine wall geometry and alters uterine geometric parameters. *(A) Representative second harmonic generation (SHG) images of uterine cross-sections from control and phthalate-exposed mice (low, medium, and high exposure groups). Scale bar = 1000 μm. (B) Endometrium (Em) total area. (C) Local circumferential myometrium (CM) thickness. Small points represent individual local thickness measurements, which were treated as individual observations in the statistical analysis; larger colored circles represent specimen means. (D) Em:CM area ratio. (E) Em:CM thickness ratio. In B, D, and E, boxplots show the median (center line), interquartile range (box), and whiskers extending to the most extreme data points within 1.5× the interquartile range; individual points represent individual specimens. Statistical comparisons were performed using one-way ANOVA followed by Tukey's post hoc test. n = 4 specimens per group for B, D, and E. *p < 0.05, **p < 0.01, ***p < 0.001, ****p < 0.0001.*

Phthalate exposure alters uterine inflation mechanics

Phthalate exposure increased uterine resistance during balloon inflation (Fig. 2A). Compared with controls, all exposure groups exhibited upward-shifted pressure–volume curves, indicating greater resistance throughout inflation. The largest increases were observed in the low and high exposure groups, whereas the medium exposure group exhibited greater specimen-to-specimen variability. Exposure-related differences were also observed in the mechanical parameters derived from the pressure–volume response (Fig. 2B–E).

Toe-region stiffness increased following phthalate exposure (Fig. 2B). Control specimens exhibited a mean toe-region stiffness of 190.4 ± 22.7 kPa/mL, compared with 336.3 ± 63.4 kPa/mL in the low group, 338.2 ± 129.0 kPa/mL in the medium group, and 400.7 ± 112.7 kPa/mL in the high group. Toe-region stiffness was significantly greater in the low and high groups than in controls, whereas the increase in the medium group did not reach statistical significance because of the larger variability.

Inflation work increased largely following phthalate exposure (Fig. 2C). Mean inflation work increased from 6.38 ± 0.75 kPa·mL in controls to 9.39 ± 1.77, 8.90 ± 2.42, and 10.55 ± 1.07 kPa·mL in the low, medium, and high groups, respectively. Significant increases were observed in the low and high groups compared with controls.

Linear-region stiffness also increased with exposure (Fig. 2D). Mean linear-region stiffness was 501.7 ± 76.9 kPa/mL in controls and increased to 609.1 ± 113.1, 553.1 ± 116.1, and 614.8 ± 70.5 kPa/mL in the low, medium, and high groups, respectively. A significant increase was observed only in the high group relative to controls.

Resistance at the final inflation volume of 0.20 mL showed a similar pattern (Fig. 2E). Final resistance increased from approximately 78 kPa in controls to 106 kPa, 98 kPa, and 113 kPa in the low, medium, and high groups, respectively. Resistance at 0.20 mL was significantly greater in the low and high groups than in controls, whereas the medium group did not differ significantly.

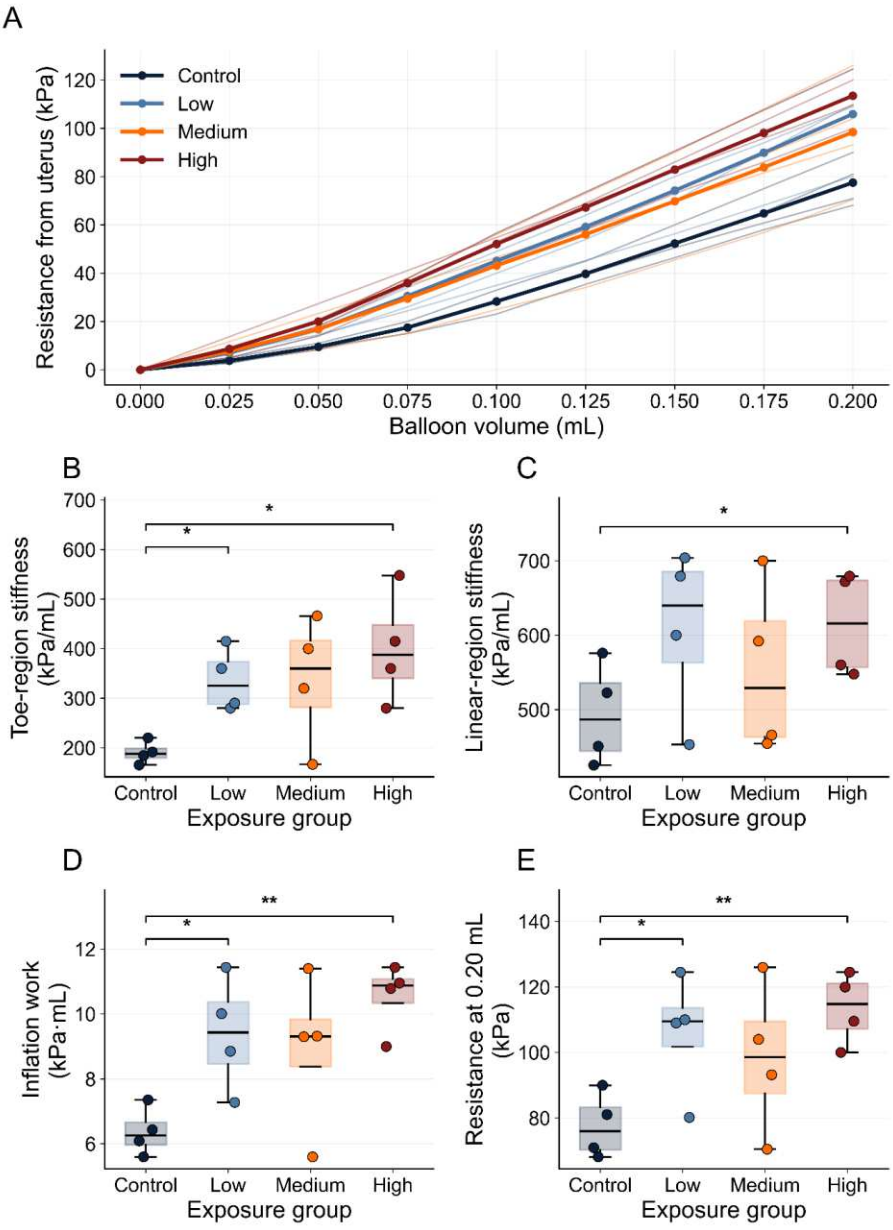


Fig. 2 Phthalate exposure alters uterine inflation mechanics. *(A) Resistance–volume curves for control and phthalate-exposed uterine horns. Thin lines represent individual specimens, and thick lines with markers represent group means. (B) Toe-region stiffness calculated from the slope of the resistance–volume response between 0 and 0.05 mL. (C) Linear-region stiffness calculated from the slope between 0.10 and 0.20 mL. (D) Inflation work, calculated as the area under the resistance–volume curve over the full inflation range from 0 to 0.20 mL. (E) Uterine resistance at the final inflation volume of 0.20 mL. Boxplots show the median (center line), interquartile range (box), and whiskers extending to the most extreme data points within 1.5× the interquartile range. Individual points represent individual specimens. Statistical comparisons were performed using one-way ANOVA followed by Tukey's honestly significant difference (HSD) post hoc test. n = 4 specimens per group. *p < 0.05, **p < 0.01.*

Uterine wall remodeling is associated with altered inflation mechanics

Correlation analysis identified consistent associations between uterine wall geometry and organ-level inflation mechanics (Fig. 3A, Supplementary Fig. S3). Total Em area and Em area fraction exhibited strong, significant negative correlations with all four mechanical parameters, whereas myometrium thickness fraction exhibited moderate positive correlations, which were significant for inflation work, linear-region stiffness, and resistance at 0.20 mL, but not for toe-region stiffness. This pattern extended across the additional structural measures (Supplementary Fig. S3), with Em-related measures generally showing negative correlations, CM-related measures showing positive correlations, and LM-related measures showing weak or nonsignificant correlations. The strongest correlations were observed for the Em:CM area and thickness ratios, both of which exhibited strong, significant negative correlations with all four mechanical parameters ($\rho = -0.66$ to -0.74).

Given the strong correlations between Em:CM area and thickness ratios and all four mechanical parameters, the Em:CM area ratio was selected to visualize these relationships in Fig. 3B–E. Lower Em:CM area ratios were associated with greater inflation work ($\rho = -0.73$; Fig. 3B), toe-region stiffness ($\rho = -0.68$; Fig. 3C), linear-region stiffness ($\rho = -0.67$; Fig. 3D), and resistance at the final inflation volume of 0.20 mL ($\rho = -0.74$; Fig. 3E).

Geometry-driven finite element (FE) simulations reproduce the experimental inflation response

Experimental and simulated ΔA–P curves exhibited similar overall inflation behavior (Fig. 4A). Experimentally, phthalate-exposed uterine horns generally exhibited reduced cross-sectional area expansion at a given pressure relative to controls, consistent with increased resistance to inflation. The FE simulations reproduced this behavior with progressive reductions in the Em:CM area and thickness ratios. The reference geometry exhibited the greatest cross-sectional area change at a given pressure, whereas the moderately and highly remodeled geometries exhibited progressively reduced expansion. Although the FE geometries were not intended to correspond directly to individual exposure groups, the simulated responses spanned the experimental range and reproduced the overall shift toward reduced expansion associated with phthalate exposure.

Parameters derived from the ΔA–P response further demonstrated agreement between the experimental and simulated inflation responses (Fig. 4B–D). Experimentally, toe-region and linear-region P–ΔA slopes generally increased with phthalate exposure, whereas ΔA–pressure AUC decreased. The same trends were reproduced by the FE simulations with increasing geometric remodeling, with progressively greater P–ΔA slopes and lower ΔA–pressure AUC from the reference to the moderately and highly remodeled geometries. The magnitudes of the simulated parameters also fell within or close to the experimental ranges, with the reference geometry approximating the control response and the remodeled geometries approaching the values observed in the phthalate-exposed groups.

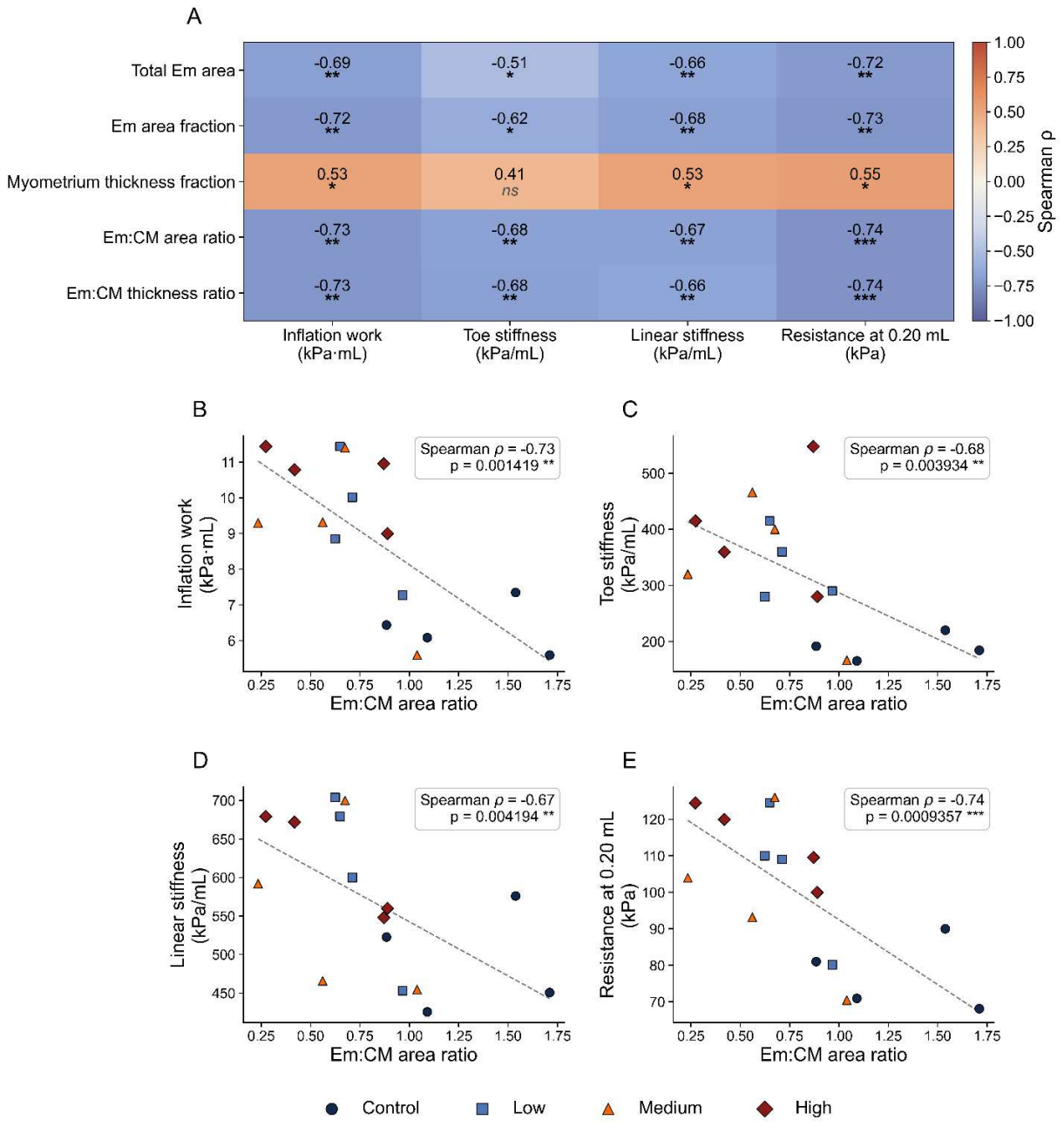


Fig. 3 Associations between uterine wall structure and organ-level inflation mechanics. *(A) Heatmap showing Spearman rank correlations between uterine geometric and mechanical parameters across all specimens. Values indicate Spearman's rank correlation coefficient (ρ), with significance determined from the corresponding correlation p-values. (B–E) Relationships between the endometrium-to-circumferential myometrium (Em:CM) area ratio and (B) inflation work, (C) toe-region stiffness, (D) linear-region stiffness, and (E) resistance at the final inflation*

*volume of 0.20 mL. Dashed lines indicate linear trend lines for visualization only; statistical inference was based on Spearman rank correlation. Points represent individual specimens and are coded by exposure group. *p < 0.05, **p < 0.01, ***p < 0.001, ns: non-significant*

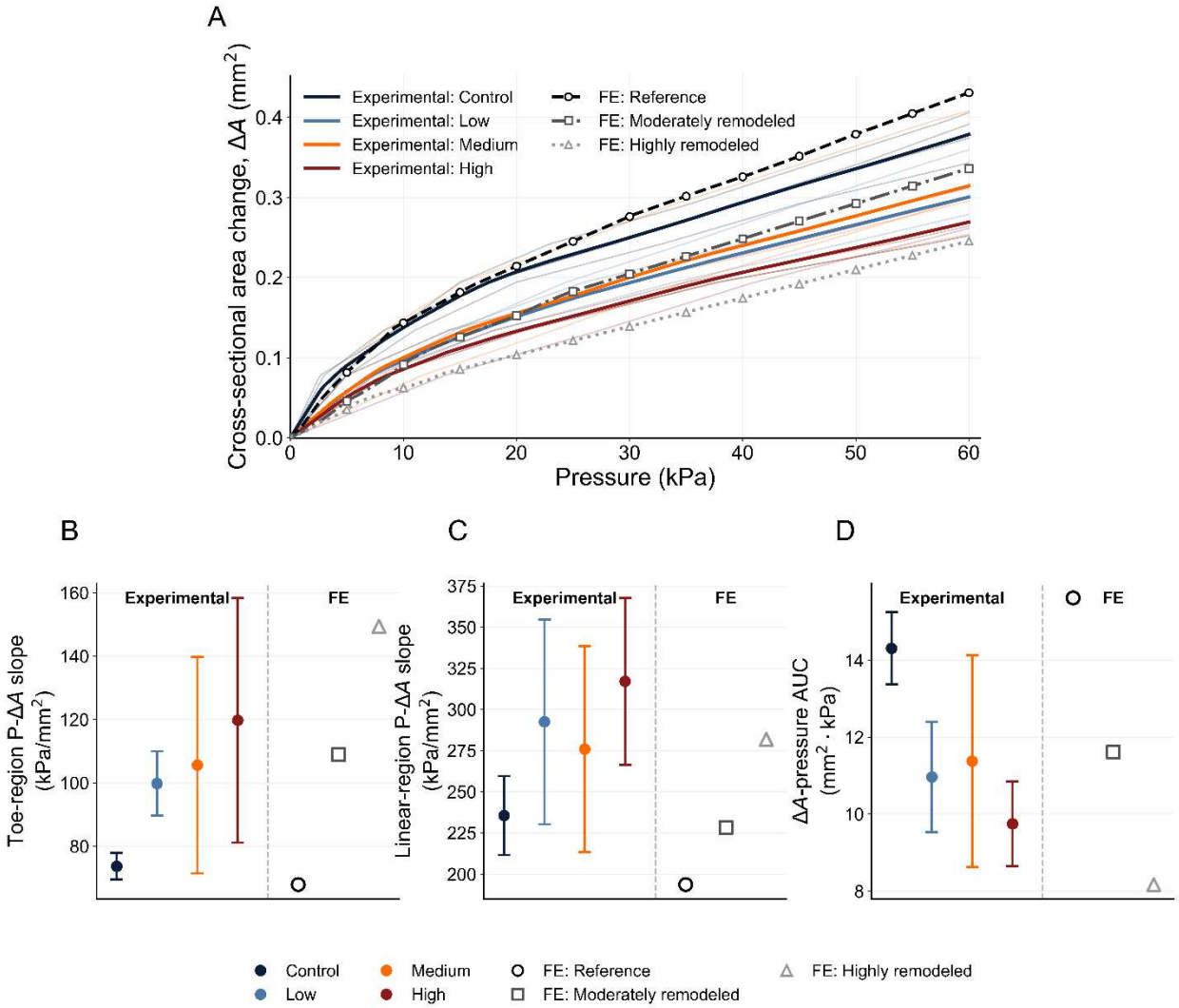


Fig. 4 *Comparison of experimental and finite element (FE) change-in-area–pressure (ΔA–P) responses. (A) Experimental ΔA–P curves for the control, low, medium, and high phthalate exposure groups and simulated ΔA–P curves for the reference, moderately remodeled, and highly remodeled geometries. Thin colored lines represent individual experimental specimens, thick colored lines represent group means, and black and gray lines with markers represent the FE simulations. (B) Toe-region P–ΔA slope. (C) Linear-region P–ΔA slope. (D) ΔA–pressure area under the curve (AUC). Experimental values in B–D are shown as mean ± SD, and individual symbols represent the corresponding FE values.*

Geometric remodeling reduces deformation and redistributes layer-specific stresses and strains

Progressive remodeling of the Em:CM geometry decreased radial displacement (Fig. 5). The reference geometry exhibited the greatest radial displacement, the highly remodeled geometry the smallest, and the moderately remodeled geometry an intermediate response throughout the circumference. The reduced global deformation was accompanied by distinct layer-specific stress and strain distributions within the uterine wall (Fig. 6).

The Em experienced the largest radial and circumferential strains of all three layers (Fig. 6A,B). With progressive Em:CM geometric remodeling, the magnitudes of the compressive radial strain and tensile circumferential strain both decreased in the Em. Mean circumferential strain decreased from approximately 6.5% in the reference geometry to 4.8% in the moderately remodeled geometry and 3.0% in the highly remodeled geometry, corresponding to an approximately 54% reduction from the reference to highly remodeled geometry. Radial stress remained compressive without a consistent monotonic trend (Fig. 6D), whereas the magnitude of the compressive circumferential stress increased with the degree of remodeling (Fig. 6C).

The CM carried the largest tensile circumferential stresses of all three layers (Fig. 6C). In contrast to the Em, circumferential stress remained tensile across all geometries and decreased in magnitude from the reference to the highly remodeled geometry (Fig. 6C). Mean circumferential stress decreased from approximately 18 kPa in the reference geometry to 16 kPa in the moderately remodeled geometry and 9 kPa in the highly remodeled geometry, representing an approximately 50% reduction from the reference to highly remodeled geometry (Figure 6C). Similar to the Em, the magnitudes of the tensile circumferential strain and compressive radial strain both decreased with remodeling (Fig. 6A, B). Compressive radial stress showed no consistent monotonic trend (Fig. 6D).

The LM exhibited comparatively low radial and circumferential stresses across all geometries (Fig. 6C, D). Both stress components remained close to zero despite relatively large circumferential and radial strains, which exceeded those in the CM (Fig. 6A, B). The magnitudes of both strain components also decreased from the reference to the highly remodeled geometry, consistent with the trends observed in the other layers.

Geometric remodeling exerts a larger influence on inflation mechanics than isolated CM stiffening

Increasing CM stiffness reduced balloon cross-sectional area change at a given applied pressure relative to the reference model, indicating increased resistance to inflation (Fig. 7A). This effect became more pronounced at higher applied pressures. In comparison, geometric remodeling produced larger reductions in cross-sectional area change throughout inflation, with the highly remodeled geometry exhibiting the greatest resistance to expansion.

Quantitative comparison of the ΔA–P-derived parameters further demonstrated differences between the effects of geometric remodeling and CM stiffening (Fig. 7B). Moderate geometric remodeling produced changes of approximately 60%, 18%, and 26% in the toe-region P–ΔA slope,

linear-region P–ΔA slope, and ΔA–pressure AUC, respectively. These changes increased to approximately 120%, 46%, and 48% for the highly remodeled geometry. In comparison, 1.5-fold CM stiffening produced corresponding changes of approximately 3%, 6%, and 9%, whereas twofold CM stiffening produced changes of approximately 6%, 16%, and 12%, respectively.

The relative effects also differed across the inflation response. Geometric remodeling produced its largest relative effect on the toe-region P–ΔA slope, whereas CM stiffening produced only small changes in the toe-region response and a greater effect on the linear-region response at higher pressures.

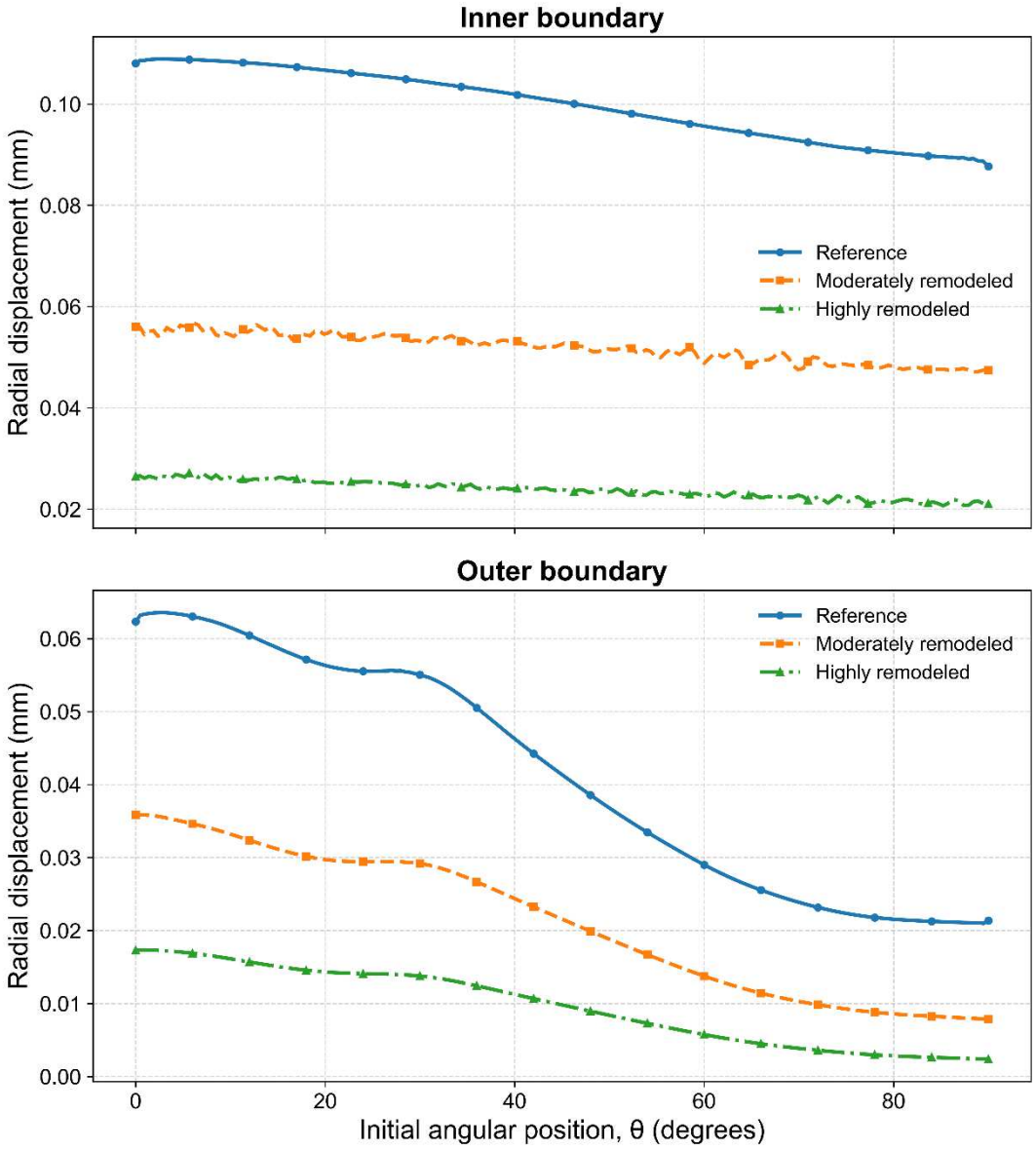


Fig. 5 *Radial displacement along the inner and outer uterine wall boundaries for reference, moderately remodeled, and strongly remodeled endometrium-to-circumferential myometrium (Em:CM) area ratio models.*

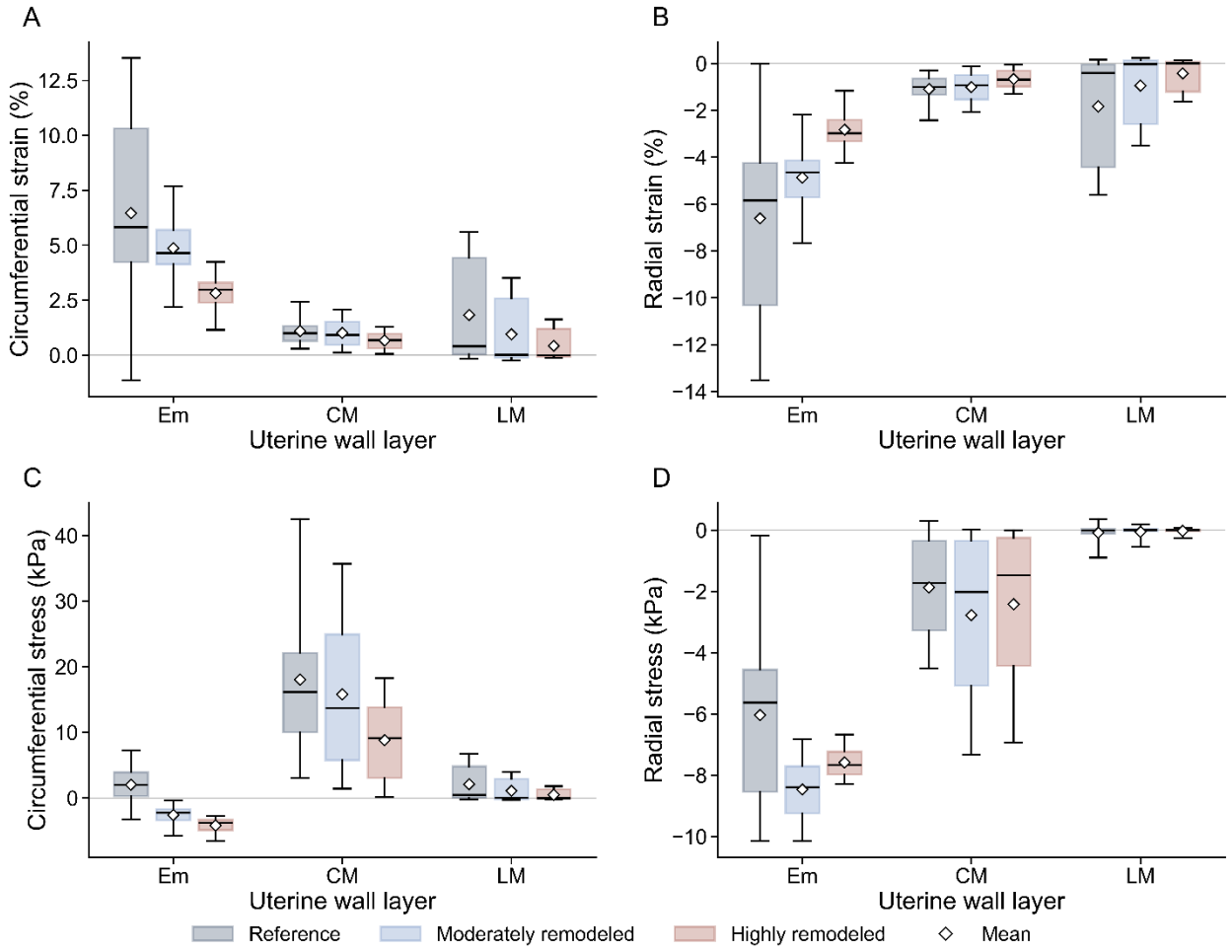


Fig. 6 Layer-specific stress and strain distributions predicted by the finite element model for the reference, moderately remodeled, and highly remodeled uterine geometries. *Box plots show the distributions of (A) circumferential strain, (B) radial strain, (C) circumferential stress, and (D) radial stress within the endometrium (Em), circumferential myometrium (CM), and longitudinal myometrium (LM). Diamonds indicate mean values. Geometric remodeling progressively altered the layer-specific mechanical response, with reduced circumferential stress and strain in the CM and reduced magnitudes of compressive radial stress and strain in the Em as the Em:CM ratio decreased.*

Discussion

The present study combined organ-level mechanical testing, quantitative geometric characterization, and image-informed FE modeling to investigate how chronic phthalate exposure alters uterine biomechanics. The findings can be summarized in three main points. First, chronic phthalate exposure remodeled uterine wall geometry toward a lower relative contribution of the Em and a greater contribution of the CM and altered organ-level inflation mechanics, with lower Em:CM ratios associated with greater resistance to inflation. Second, FE simulations demonstrated that geometric remodeling alone, while maintaining identical constitutive properties, reproduced

the experimentally observed shift toward increased inflation resistance and revealed that this response was accompanied by reduced wall deformation and redistribution of layer-specific stresses and strains. Third, geometric remodeling had greater influence on inflation mechanics than experimentally motivated increases in CM stiffness, with CM stiffening having a comparatively small effect overall and an even smaller effect in the toe region. Together, these findings identify uterine wall geometry as an important determinant of passive inflation mechanics and provide a mechanistic framework linking phthalate-induced geometric remodeling to altered organ-level mechanical behavior.

In the present study, SHG imaging demonstrated significant remodeling of uterine wall geometry following chronic phthalate exposure, characterized by reduced Em area, increased CM thickness, and corresponding reductions in the Em:CM area and thickness ratios (Fig. 8). These geometric changes were accompanied by significantly increased resistance during balloon inflation (Fig. 2), demonstrating that chronic phthalate exposure alters both uterine wall geometry and passive organ-level mechanical behavior. Since the uterus undergoes substantial mechanical loading and deformation during implantation, pregnancy, and parturition, alterations in its passive mechanical behavior may influence its ability to accommodate physiological loading, providing a functional consequence of environmentally induced tissue remodeling beyond previously reported histological changes.

The altered mechanical response was evident throughout inflation and was reflected across all four parameters derived from the pressure–volume response (Fig. 2). Toe-region stiffness, linear-region stiffness, inflation work, and final inflation resistance all showed an increasing pattern following phthalate exposure. These changes indicate an overall increase in uterine resistance throughout inflation following chronic phthalate exposure.

Uterine wall geometry was also closely associated with the measured inflation mechanics (Fig. 3). Several geometric parameters were significantly correlated with the mechanical response, with the Em:CM area and thickness ratios showing the strongest correlations across all four mechanical parameters. Lower Em:CM ratios were associated with greater toe-region stiffness, linear-region stiffness, inflation work, and final inflation resistance. Because the Em:CM ratios captured the relative geometric redistribution between the Em and CM and showed the strongest relationships with the overall inflation response, they were selected as the basis for the subsequent FE analysis.

While these experimental observations established strong relationships between uterine wall geometry and inflation mechanics, they could not determine whether geometric remodeling itself caused the altered mechanical response because chronic phthalate exposure may simultaneously induce biological changes that affect tissue material properties. To isolate the contribution of wall geometry, image-informed FE simulations were performed in which only the relative thicknesses of the Em and CM were varied while all constitutive properties, loading conditions, and boundary conditions remained unchanged.

The simulated geometries represented increasing degrees of remodeling based on the range of Em:CM ratios observed across the experimental groups. Progressive reductions in the Em:CM ratio reproduced the experimental pressure–Δarea trend and spanned the range of measured responses (Fig. 4), with remodeled geometries requiring greater pressure to achieve the same degree of expansion. Because constitutive properties and all other model conditions were held constant, these results demonstrate that geometric remodeling within the experimentally observed range can independently produce increases in resistance to inflation.

The relative influence of geometric remodeling was further evaluated against experimentally motivated increases in CM stiffness (Fig. 7). Increasing CM fiber stiffness by 1.5- and 2.0-fold increased resistance to expansion, but the resulting changes were much smaller than those produced by geometric remodeling. This difference was particularly pronounced in the toe region, where CM stiffening produced only minor changes compared with the large effect of geometric remodeling. These findings indicate that, within the ranges examined, uterine inflation mechanics were considerably more sensitive to geometric remodeling than to isolated changes in CM stiffness.

Having established that geometric remodeling alone reproduced the organ-level inflation behavior, the FE analyses further provide insight into the underlying mechanical mechanisms. Progressive Em:CM geometric remodeling decreased radial displacement (Fig. 5) and redistributed the internal mechanical environment of the uterine wall (Fig. 6). The CM consistently carried the greatest tensile circumferential stress, consistent with its predominantly circumferential collagen organization and supporting its role as the principal load-bearing layer during inflation. In contrast, the LM exhibited negligible circumferential and radial stresses despite relatively large strains in both directions (Fig. 6). This stress–strain distinction likely reflects the predominantly longitudinal collagen organization of the LM, which provides less resistance to circumferential and radial deformation, allowing the LM to deform with the expanding uterine wall.

The Em exhibited a qualitatively different response (Fig. 6). Despite undergoing positive circumferential strain, consistent with outward radial expansion of the uterine wall, the corresponding circumferential stress remained predominantly compressive. Abaqus reports the hydrostatic pressure, p and total circumferential Cauchy stress, $\sigma_{\theta\theta}$. The deformation-related (deviatoric) circumferential stress was therefore obtained using the standard decomposition,

$$\sigma_{\theta\theta} = -p + \sigma_{\theta\theta}^{\mathrm{dev}},$$

where $\sigma_{\theta\theta}^{\mathrm{dev}}$ is the deformation-related (deviatoric) circumferential stress. This analysis showed that the deformation-related circumferential stress remained tensile, as expected from the positive circumferential strain, but was outweighed by a larger compressive hydrostatic pressure. This pressure developed because the nearly incompressible Em was simultaneously compressed by the expanding balloon and mechanically confined by the surrounding CM, limiting its ability to

deform freely. Consequently, the Em experienced net compressive circumferential stress despite undergoing circumferential extension.

An important implication of these findings is that geometric remodeling represents an additional mechanism through which environmental toxicants may alter organ-level biomechanics. More broadly, alterations in the relative thicknesses of the Em and myometrium are not unique to phthalate exposure and have also been reported in other environmental exposures and uterine pathologies [14, 36–40]. The present findings therefore suggest that geometric remodeling of the uterine wall may represent a common biomechanical mechanism through which diverse conditions influence uterine mechanical function. These findings also highlight the importance of representing the uterus as a layered structure in computational models. Although two uterine walls may have similar overall dimensions, differences in the relative thicknesses of the Em and myometrium can considerably alter uterine resistance to distension and the internal distribution of stresses and strains. Consequently, treating the uterine wall as a homogeneous tissue may overlook important mechanical effects arising from layer-specific remodeling.

The present study demonstrates that redistribution of uterine wall geometry alone is sufficient to reproduce the experimentally observed inflation trend and alter deformation and internal stress distributions, even when constitutive parameters remain unchanged. Importantly, remodeling of the relative Em and myometrial compartments may have biological consequences beyond these changes in passive organ-level mechanics. The Em and myometrium perform distinct and non-interchangeable reproductive functions. The Em provides the specialized epithelial and stromal environment required for embryo attachment and implantation [41–43]. Following implantation, endometrial stromal cells undergo decidualization, accompanied by extensive extracellular matrix remodeling, angiogenesis, and immunomodulatory changes that support early pregnancy [42, 44]. A reduction in the relative Em compartment may therefore have functional consequences by reducing the tissue available to support these biological processes that are crucial for successful pregnancy.

At the same time, geometric remodeling alters the distribution of stress and strain within the uterine wall and therefore the local mechanical environment experienced by cells within individual tissue compartments. Myometrial smooth muscle cells are mechanosensitive, and mechanical stretch has been shown to activate intracellular signaling pathways and regulate downstream transcriptional, inflammatory, and contraction-associated responses [45–50]. Consequently, remodeling-induced changes in myometrial stress and strain could potentially modify mechanotransductive signaling and cellular adaptation. Although these downstream biological responses were not evaluated in the present study, the findings suggest that altered uterine wall geometry could influence reproductive function through two complementary mechanisms: by changing the relative availability of functionally specialized tissue compartments and by modifying the mechanical cues experienced by cells within those compartments. Together, these findings demonstrate that uterine wall geometry is a key determinant of both organ-level mechanical behavior and the local mechanical

environment, providing a link between structural remodeling and potential changes in uterine function.

Several limitations should be considered when interpreting these findings. Layer-specific material properties were not directly measured or independently identified through inverse analysis. Instead, the constitutive parameters were based on values obtained from a previous study using a homogeneous uterine tissue assumption, with C_{10} and k_2 held constant across layers and k_1 scaled according to relative SHG intensity [51]. Because the parameters obtained from the homogeneous-wall model represent effective whole-wall properties, some overlap may exist between the collagen-associated stiffness captured by C_{10} and the explicit fiber contribution assigned to the endometrium through k_1 in the layered model. Therefore, these parameter assignments should not be interpreted as a unique decomposition of layer-specific matrix and collagen contributions.

Although the CM stiffness sensitivity analysis evaluated the influence of potential changes in material properties, the model did not incorporate layer-specific property changes measured from the specimens examined in the present study. The model also represented only the passive mechanical response of the uterine wall and did not account for active smooth muscle contraction. In vivo, active myometrial contraction generates additional stresses within the uterine wall and could alter both resistance to distension and the distribution of stress and strain among the uterine layers. The stress and strain distributions predicted here should therefore be interpreted as those associated with passive inflation rather than as representative of an actively contracting uterus.

The comparison between the experimental and computational inflation responses also suggests that remodeling may alter the nonlinear mechanical behavior of the uterine wall. Although geometric remodeling reproduced much of the overall increase in resistance to inflation, the model showed different degrees of overprediction and underprediction across the deformation range. This strain-dependent discrepancy suggests that geometric remodeling alone does not fully capture how uterine resistance changes with increasing deformation and and further suggests that alterations in tissue material behavior may also contribute to the experimental response. Future studies incorporating experimentally determined layer-specific constitutive properties could help distinguish the contributions of geometric remodeling from changes in material nonlinearity.

In addition, the model used a two-dimensional plane-strain approximation of a transverse uterine cross-section. This formulation does not capture longitudinal deformation or spatial variations in geometry along the uterine horn, both of which could redistribute load and affect the absolute magnitudes and spatial distributions of the predicted stresses and strains. Accordingly, the layer-specific mechanical fields should be interpreted within the context of the two-dimensional model rather than as complete three-dimensional representations of uterine mechanics. However, because the same assumptions were maintained across all geometry and material-property

variation cases, the simulations provide a consistent framework for evaluating the relative effects of geometric remodeling and CM stiffening. Despite these limitations, computational simulations reproduced the inflation responses of the control and exposed groups reasonably well and captured the remodeling-associated changes in organ-level mechanical behavior.

Together, the experimental and computational findings establish uterine wall geometry as an important contributor to passive organ-level mechanics and provide a mechanistic connection between exposure-associated structural remodeling and altered uterine biomechanics. These findings emphasize the importance of considering layered tissue architecture when evaluating how uterine remodeling affects mechanical function.

Methods

1. Experimental procedures

1.1 Animal exposure and uterine tissue collection

Adult female mice were chronically exposed to either vehicle control or a phthalate mixture at low, medium, or high exposure levels. The treatment groups consisted of Control, Low, Medium, and High exposure groups, corresponding to phthalate-mixture concentrations of 0, 0.15, 1.5, and 1500 ppm, respectively. Each experimental group consisted of four animals, with one uterine horn collected from each animal for subsequent mechanical testing and imaging (n = 4 uterine horns per group). Animals were exposed for 1 year using dietary administration [18]. All animal experiments were approved by the Institutional Animal Care and Use Committee (IACUC) at the University of Illinois Urbana-Champaign and were performed in accordance with institutional guidelines and the Guide for the Care and Use of Laboratory Animals.

At end of the 1-year exposure, animals were euthanized at diestrus, and the reproductive tract was collected. Individual uterine horns were isolated by carefully removing the surrounding adipose and connective tissues while preserving the uterine wall. Samples were maintained in Krebs buffer during tissue preparation and remained immersed in Krebs buffer throughout balloon inflation testing to minimize tissue dehydration. One uterine horn from each animal was used for balloon inflation testing and imaging as described below.

1.2 Balloon inflation testing

Organ-level mechanical behavior was characterized by using a volume-controlled balloon inflation system we have used in a previous study [51]. A compliant balloon catheter with glycerol lubrication was inserted into the uterine lumen and positioned within the central portion of the uterine horn.

The catheter was connected to a syringe pump that delivered fluid at a controlled rate of 0.02 mL/min. A second, identical catheter open to atmospheric pressure was used as a reference. The inflation and reference lines were connected to a differential pressure sensor, allowing the pressure required to inflate the balloon alone to be removed from the measured response. The resulting

differential pressure therefore represented the resistance generated by the uterine tissue during balloon expansion.

Before data acquisition, each specimen was preconditioned using three inflation–deflation cycles to a maximum injected volume of 0.20 mL. Following preconditioning, the balloon was inflated from 0 to 0.20 mL in increments of 0.025 mL. Pressure was recorded continuously at 1 Hz using an Arduino-based acquisition system. At each prescribed volume, inflation was paused for 1 minute before the corresponding pressure was recorded. Krebs buffer was periodically applied to the tissue surface throughout testing to maintain hydration.

The measured pressure is referred to as uterine inflation resistance because it represents the pressure difference between the tissue inflated by the balloon and the reference balloon. Resistance–volume curves were generated for each specimen by plotting the measured uterine resistance against the cumulative balloon volume.

1.3 Second harmonic generation (SHG) imaging

Uterine wall structure was characterized using SHG microscopy. An approximately 1 cm segment of each uterine horn was isolated for balloon inflation testing. The remaining portion of the same uterine horn was embedded, cryosectioned, and used for SHG imaging and analysis. Images used to quantify uterine wall geometry were obtained from tissue prior to inflation. Each uterine horn was imaged in cross-section using a Zeiss LSM 980 equipped with a 20× objective. SHG signal was collected using an excitation wavelength of 780 nm. Images were acquired as tiled cross-sectional scans encompassing the entire uterine cross-section. Identical imaging settings, including laser power and detector gain, were used for all specimens.

2. Experimental data analysis

2.1 Image segmentation and geometric quantification

SHG images were processed using Fiji, ImageJ. The uterine wall was divided into three anatomical compartments: Em, CM, and LM. The boundaries between the Em, CM, and LM were manually delineated based on visual differences in tissue morphology, collagen organization, and smooth muscle orientation observed in the SHG images. Separate binary masks were generated for the 3 layers. Disconnected regions outside the uterine wall were excluded before quantitative analysis.

Custom Python scripts were used to quantify geometric parameters, including layer areas, area fractions, and layer thicknesses, from the segmented masks. All area and thickness measurements were calculated in pixel-based units. Pixel dimensions were converted to micrometers using the microscope calibration associated with each image.

Cross-sectional area measurements: The cross-sectional areas of the Em, CM, and LM were calculated by counting the number of pixels contained within the corresponding binary masks and are denoted as A_{Em}, A_{CM}, A_{LM}, respectively. The Em area fraction was calculated as the Em cross-

sectional area relative to the total uterine wall cross-sectional area: $f_{\mathrm{Em,area}} = \frac{A_{\mathrm{Em}}}{A_{\mathrm{Em}}+A_{\mathrm{CM}}+A_{\mathrm{LM}}}$. The relative cross-sectional areas of the Em and CM were additionally characterized using the Em:CM area ratio: $R_{\mathrm{Em:CM,area}} = \frac{A_{\mathrm{Em}}}{A_{\mathrm{CM}}}$

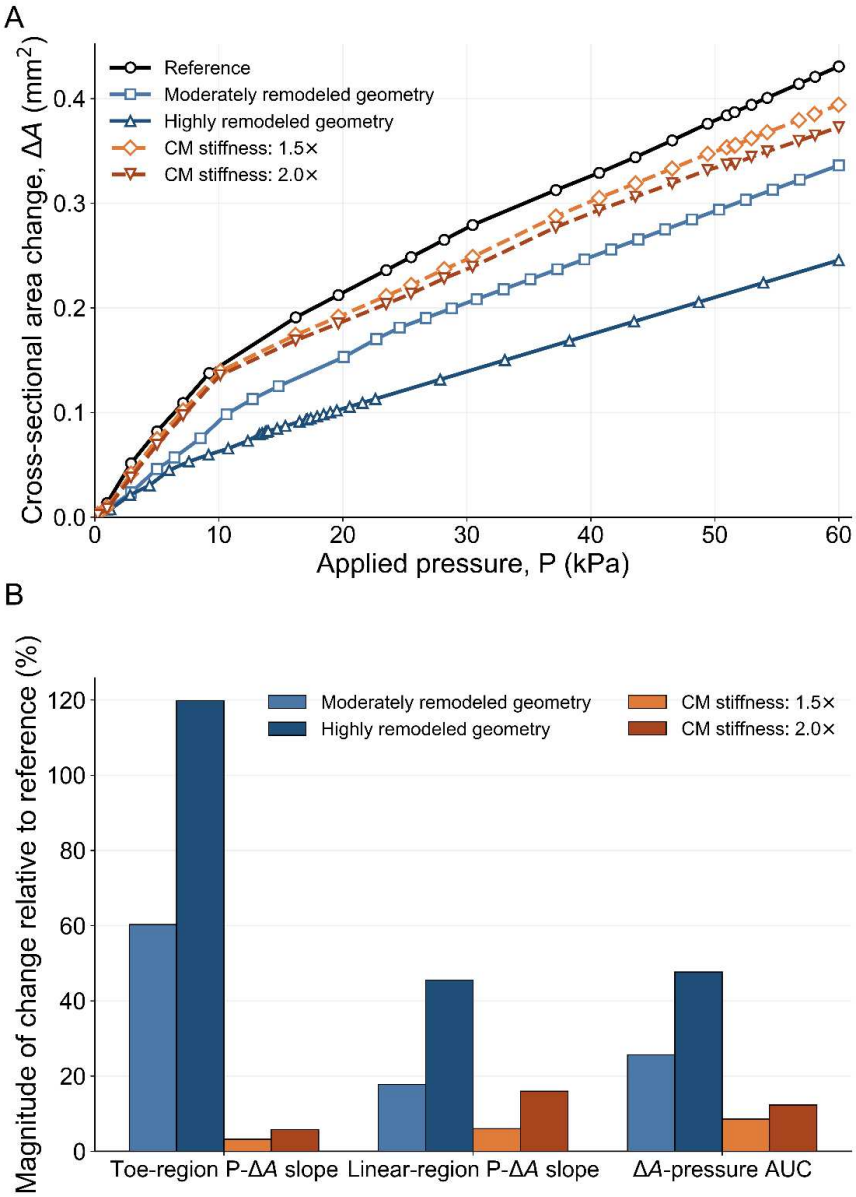


Fig. *7 Independent effects of geometric remodeling and circumferential myometrium (CM) stiffening on the simulated uterine inflation response. (A) Simulated cross-sectional area change (ΔA) as a function of applied pressure for the reference, moderately remodeled, and highly remodeled geometries and for models with 1.5× and 2.0× increases in CM stiffness while maintaining the reference geometry. (B) Magnitude of percent change in the ΔA–P-derived parameters relative to the reference model, including toe-region P–ΔA slope, linear-region P–ΔA slope, and ΔA–pressure area under the curve (AUC).*

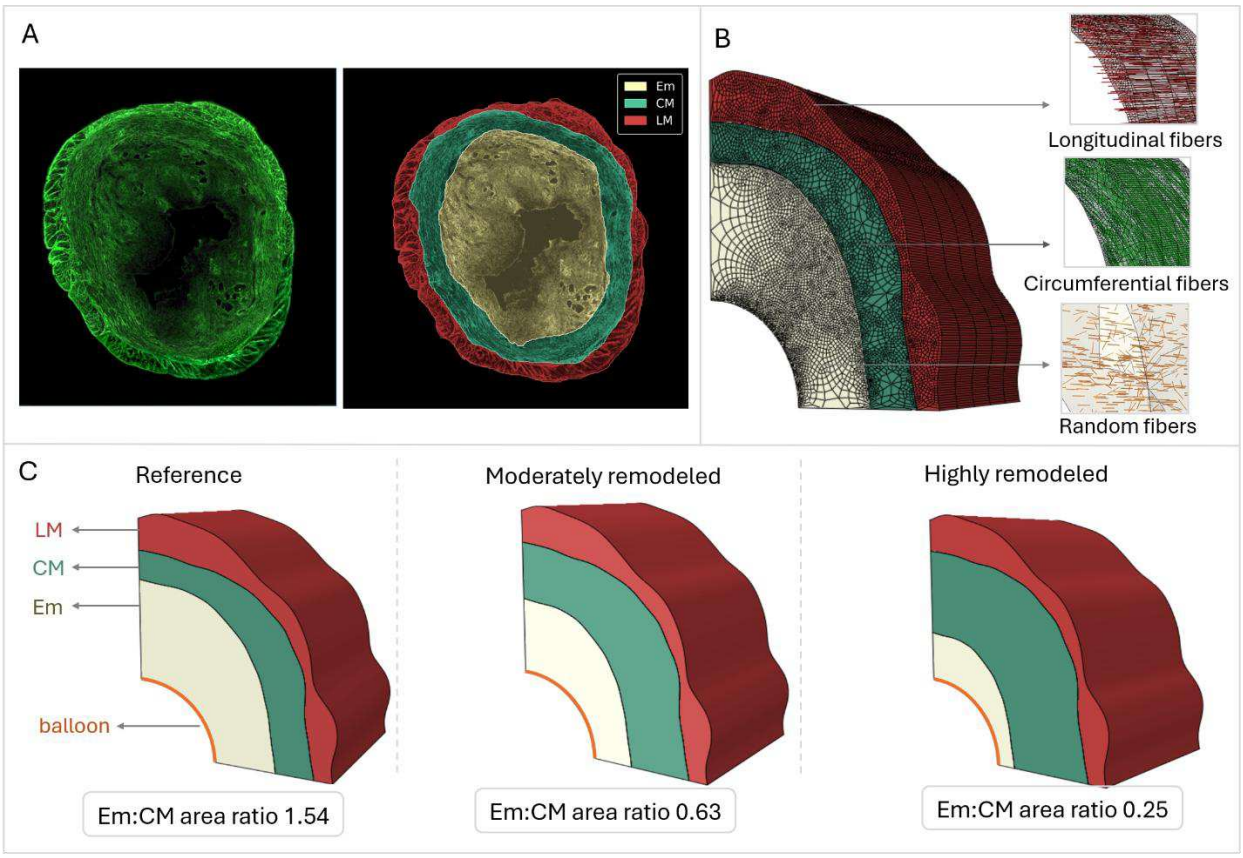


Fig. 8 Development of layered finite element models of the uterine wall. *(A) Representative second harmonic generation (SHG) image of the uterine cross-section and corresponding segmentation into the endometrium (Em), circumferential myometrium (CM), and longitudinal myometrium (LM). (B) Quarter-symmetry finite element (FE) model showing the assigned layer-specific fiber orientations. The LM was assigned a longitudinal fiber orientation, the CM a circumferential fiber orientation, and the Em an isotropic fiber distribution with no preferred orientation. (C) Three FE models representing the reference, moderately remodeled, and highly remodeled uterine wall geometries. Geometric remodeling was simulated by progressively reducing the Em:CM area ratio while preserving the overall uterine wall dimensions, resulting in Em:CM area ratios of 1.54, 0.63, and 0.25 for reference, moderately remodeled, and highly remodeled geometries, respectively.*

Layer thickness measurements: Local layer thickness was quantified from each segmented layer mask using a medial-axis-based thickness algorithm implemented in custom Python scripts. For each binary mask, a medial axis (skeleton) representing the centerline of the segmented tissue compartment was generated. The Euclidean distance from each medial-axis point to the nearest mask boundary was calculated using a distance transform, and local thickness was defined as twice this distance.

To account for spatial variation in layer thickness, 50 local thickness values were sampled uniformly along the medial axis of each specimen and used for subsequent statistical analyses. Mean layer thickness was additionally calculated for each specimen as the average of the sampled local thickness values, yielding $\bar{t}_{\mathrm{Em}}$, $\bar{t}_{\mathrm{CM}}$, $\bar{t}_{\mathrm{LM}}$.

The relative thicknesses of the Em and CM were characterized using the Em:CM thickness ratio:

$$R_{\mathrm{Em:CM,thickness}} = \frac{\bar{t}_{\mathrm{Em}}}{\bar{t}_{\mathrm{CM}}}$$

The relative contribution of the myometrium to the overall uterine wall thickness was characterized using the myometrial thickness fraction:

$$f_{\mathrm{Myo,thickness}} = \frac{\bar{t}_{\mathrm{CM}} + \bar{t}_{\mathrm{LM}}}{\bar{t}_{\mathrm{Em}} + \bar{t}_{\mathrm{CM}} + \bar{t}_{\mathrm{LM}}}.$$

2.2 Pressure–volume data processing

The baseline pressure measured at zero injected volume was subtracted from each recording so that the resistance–volume response began at zero.

Inflation work: The total mechanical work associated with uterine inflation was quantified as the area under the resistance–volume curve from 0 to 0.20 mL. Numerical integration was performed using the trapezoidal rule:

$$W_{\mathrm{inflation}} = \sum_{i=1}^{n-1} \frac{P_i + P_{i+1}}{2} (V_{i+1} - V_i),$$

where P_i and P_{i+1} are consecutive resistance measurements and $V_i$and V_{i+1} are the corresponding balloon volumes.

Toe-region stiffness: Toe-region stiffness was used to characterize the initial resistance of the uterine wall to inflation. Consistent with previous biomechanical studies that quantify the slope of the initial toe region of nonlinear soft-tissue responses [52, 53], a linear regression was fitted to the initial toe region of the resistance–volume response between 0 and 0.05 mL to provide a quantitative measure of the average initial stiffness:

$$P = k_{\mathrm{toe}} V + b,$$

where k_{toe} (kPa/mL) is the toe-region stiffness.

Linear-region stiffness: Linear-region stiffness was calculated from the approximately linear portion of the resistance–volume curve between 0.10 and 0.20 mL. A least-squares linear regression was fitted to the measurements within this volume range:

$$P = k_{\text{linear}} V + b,$$

where k_{linear} (kPa/mL) is the linear-region stiffness.

Final inflation resistance: Final inflation resistance was defined as the uterine resistance measured at the final prescribed inflation volume of 0.20 mL:

$$P_{\text{final}} = P(V = 0.20 \text{ mL}).$$

2.3 Statistical analysis

Statistical analyses were performed using Python with the SciPy and statsmodels libraries. Each uterine horn was treated as an independent experimental specimen, and data were grouped according to Control, Low, Medium, and High phthalate exposure. For specimen-level geometric and mechanical parameters, statistical analyses were performed using one value per uterine horn. For local CM thickness, individual measurements across the tissue section were retained to preserve spatial variability that would otherwise be obscured by a single specimen-level mean. Data normality within each group was assessed using the Shapiro–Wilk test, and homogeneity of variance was evaluated using Levene's test centered on the median. Differences among the four exposure groups were evaluated using one-way analysis of variance (ANOVA), followed by Tukey's honestly significant difference (HSD) test for pairwise comparisons. Statistical significance was defined as $p < 0.05$.

Associations between geometric and mechanical parameters were evaluated across all specimens using Spearman rank-order correlation. Geometric parameters included Em area, CM area, LM area, Em area fraction, mean Em thickness, mean CM thickness, local Em thickness, local CM thickness, and the Em:CM area and thickness ratios. Mechanical parameters included inflation work, toe-region stiffness, linear-region stiffness, and final inflation resistance at 0.20 mL. For each geometric–mechanical parameter pair, Spearman's rank correlation coefficient (ρ) and associated p-value were calculated. Correlation coefficients were visualized using a heatmap, and selected associations were additionally displayed as specimen-level scatter plots. Ordinary least-squares trend lines were included for visualization only; all statistical inference was based on Spearman correlation.

3. Image informed Finite element model development

3.1 Image-based reconstruction of the layered uterine wall

A specimen-specific three-layer FE model of the uterine wall was developed from SHG images. The uterine wall was segmented into three anatomically distinct regions consisting of the Em, CM,

and LM. Binary masks were generated for each tissue layer using the segmented SHG images (Fig. 8A). The interfaces between adjacent layers were defined using shared boundaries to ensure continuous geometric transitions between the Em, CM, and LM. Following segmentation, the contours corresponding to the Em outer boundary, CM outer boundary, and LM outer boundary were extracted and smoothed to remove pixel-level irregularities while preserving the overall tissue morphology.

The extracted contours were imported into FreeCAD, where spline curves were generated for each boundary and used to reconstruct the layered uterine wall geometry. The reconstructed geometry was then exported as a STEP file and imported into Abaqus/CAE for FE model generation.

3.2 FE model development

The reconstructed layered uterine geometry was incorporated into the previously developed and validated FE inflation framework [51]. Consistent with the previous model, a quarter-symmetry representation of the uterine cross-section was used, with the balloon positioned within the uterine lumen and described using the independently calibrated Ogden constitutive model. Surface-to-surface contact was defined between the balloon and Em using a finite-sliding formulation with a friction coefficient of $\mu_f = 0.03$. Symmetry boundary conditions were applied along the two symmetry planes, and axial displacement was constrained to approximate plane-strain conditions.

All simulations used identical mesh density, loading conditions, contact definitions, and boundary conditions. Mesh convergence was evaluated by comparing radial displacement along the inner and outer uterine wall contours across coarse, reference, and fine meshes, with the reference mesh selected to balance numerical convergence and computational cost (Supplementary Fig. S4).

Constitutive model: All tissue layers were modeled using the built-in Abaqus implementation of the one-fiber-family Gasser–Ogden–Holzapfel (GOH) hyperelastic constitutive model. The strain-energy density function is given by

$$\Psi = C_{10}(\bar{I}_1 - 3) + \frac{k_1}{2k_2}[\exp(k_2[\kappa(\bar{I}_1 - 3) + (1 - 3\kappa)(\bar{I}_4 - 1)]^2) - 1] + \Psi_{\text{vol}}(J) \quad (1)$$

Here, C_{10} represents the isotropic ground-matrix stiffness, k_1 governs the fiber stiffness, k_2 controls the nonlinear exponential stiffening of the fibers, and κ is the fiber dispersion parameter, where κ = 0 corresponds to perfectly aligned fibers and κ= 1/3 represents an isotropic fiber distribution. The invariant $\bar{I}_4 = a_0 \cdot \bar{C} a_0$ describes the squared stretch along the preferred fiber direction. The volumetric strain-energy term, Ψ_{vol}, enforces incompressibility through the volume ratio $J = 1$. Because the tissue layers were modeled as incompressible, a hybrid finite-element formulation was used to avoid volumetric locking. In the hybrid formulation, hydrostatic pressure, p, is introduced as an independent solution variable associated with enforcement of the incompressibility constraint. Hydrostatic pressure was obtained from the Abaqus field output variable PRESS, for which positive values represent compression.

Layer-specific constitutive property assignment:

The baseline GOH material parameters were adopted from the previously developed homogeneous inverse FE model [51]. The isotropic parameter C_{10} and fiber nonlinearity parameter k_2 were held constant across all uterine layers, whereas the fiber stiffness parameter k_1 was assigned on a layer-specific basis using SHG measurements (table 1).

Layer-specific k_1 values for the Em and CM were assigned based on relative SHG intensity. The parameter k_1 governs the stiffness contribution of the collagen fiber families [54], whereas SHG intensity has been used as a measure of relative fibrillar collagen density [55, 56]. The homogeneous k_1 obtained from the previous inverse FE analysis was therefore scaled according to the ratio of each layer's mean SHG intensity to the mean intensity of the combined Em–CM region:

$$k_1^{\text{layer}} = k_1^{\text{hom}} \left(\frac{I_{\text{layer}}}{I_{\text{Em-CM}}} \right) \tag{2}$$

Where k_1^{hom} is the homogeneous fiber stiffness parameter obtained from the previous inverse FE analysis, I_{layer} is the mean SHG intensity of the Em or CM, and $I_{\text{Em-CM}}$ is the mean SHG intensity of the combined Em–CM region. The combined Em–CM region was used as the normalization reference because the baseline homogeneous k_1 represented the mechanical response of this composite tissue. This approach accounted for the lower collagen-associated SHG signal observed in the Em relative to the CM.

The LM was excluded from the SHG-based normalization because its collagen fibers are oriented predominantly along the longitudinal axis of the uterine horn and are therefore largely out of the imaging plane in transverse SHG sections. SHG signal intensity is sensitive to collagen fiber orientation relative to the imaging plane, and out-of-plane fibers may generate reduced signal [55]. Consequently, the measured SHG intensity of this layer is expected to underestimate its true collagen content and was not considered appropriate for parameter scaling. Instead, the LM was assigned the same constitutive parameters as the CM, reflecting the similar collagen-rich composition of the two myometrial layers while avoiding parameter assignment based on an orientation-dependent SHG signal.

Because a quantitative constitutive relationship between SHG intensity and k_1 has not been established for uterine tissue, the proportional relationship between normalized SHG intensity and k_1 used in Eq. (2) is a modeling assumption.

Layer-specific collagen fiber orientation and dispersion were assigned based on SHG measurements (Fig. 7B). Collagen fiber dispersion was quantified using spherical variance (SV). The measured SV for each layer was converted to the GOH fiber dispersion parameter (κ) using the previously established mapping relationship [51]. Within the one-fiber-family GOH formulation, the preferred fiber direction was defined by the unit vector a_0 in a local material coordinate system assigned to each layer. For the CM, the preferred fiber direction was aligned

with the circumferential basis vector, $a_0 = e_\theta$, whereas for the LM, fibers were aligned with the longitudinal basis vector, $a_0 = e_z$. The Em was also represented using a single fiber family but was assigned a high fiber dispersion parameter (κ), reflecting its more dispersed collagen organization and resulting in a nearly isotropic mechanical response despite the presence of collagen fibers. The layer-specific fiber orientations and dispersion parameters used in the model are summarized in Table 1.

Table 1 summarizes the assignment of the GOH constitutive parameters.

Parameter	Assignment method	Assignment
a_0	Layer-specific orientation measured from SHG	$a_0 = e_\theta$ (CM) $a_0 = e_z$ (LM) $a_0 = e_z$ (Em)
κ	Calculated from spherical variance	0.05 (CM and LM) 0.25 (Em)
C_{10}	Adopted from previous work [51]; constant across layers	15 kPa
k_1	Scaled from previous work [51] according to normalized SHG intensity	461.55 kPa (CM and LM) 231.31 kPa (Em)
k_2	Adopted from previous work [51]; constant across layers	9

4. Finite Element simulation analyses

4.1 Em:CM thickness redistribution

To investigate the influence of uterine wall geometry on inflation mechanics independently of tissue material properties, the relative Em:CM geometry was systematically varied while maintaining a constant total uterine wall cross-sectional area, LM area, constitutive material properties, loading conditions, and boundary conditions. Consequently, differences in the predicted mechanical response reflected only changes in the relative geometry of the Em and CM.

The modeled geometries were based on experimentally measured Em:CM thickness and area ratios obtained from SHG image analysis. Three geometries were selected to span the full range of specimen-level values observed across the control and phthalate-exposed groups, including the experimentally measured minimum and maximum ratios. Control specimens generally exhibited the highest ratios, whereas phthalate-exposed specimens exhibited progressively lower ratios, with the medium- and high-exposure groups showing significantly reduced values.

The reference geometry had an Em:CM thickness ratio of 4.56 and an Em:CM area ratio of 1.54, corresponding to the upper end of the experimentally observed range. The moderately remodeled geometry had thickness and area ratios of 2.31 and 0.63, respectively, while the highly remodeled geometry had corresponding ratios of 1.35 and 0.25, representing the lower end of the

experimentally observed range. Together, these geometries spanned the range of Em:CM geometric remodeling observed experimentally (Fig. 7C).

The Em:CM thickness and area ratios reported throughout this study correspond to the pre-inflation uterine geometry measured from the SHG images and were used as target ratios during model construction. To reproduce the experimental inflation configuration, however, the FE model explicitly included the balloon within the uterine lumen. Consequently, the innermost 0.5 mm of the measured Em was represented by the balloon rather than meshed as tissue. Although this reduced the meshed Em thickness adjacent to the lumen, the reported Em:CM ratios correspond to the original pre-inflation geometry, thereby allowing direct comparison between the modeled geometries and the experimental SHG measurements.

4.2 Generation of experimental and simulated pressure–area curves

Since the FE model represented a transverse uterine cross-section under plane-strain conditions, the experimental and simulated inflation responses were compared based on changes in balloon cross-sectional area (ΔA) rather than inflation volume. Experimental balloon volumes were therefore converted to equivalent cross-sectional areas using an experimentally determined balloon volume–diameter calibration (Supplementary Fig. S5).

For the experimental data, balloon diameter at each prescribed inflation volume was obtained by linear interpolation of the measured volume–diameter calibration. The corresponding balloon cross-sectional area was calculated assuming a circular cross-section:

$$A_i = \pi \left(\frac{D_i}{2} \right)^2$$

Where D_i is the interpolated balloon diameter and A_i is the corresponding cross-sectional area at inflation increment i. The experimentally measured uterine inflation resistance at each volume increment was then paired with the corresponding calculated area. Because the differential pressure measurements accounted for the pressure required to inflate the balloon alone, the measured pressure represented the resistance associated with inflation within the uterine tissue.

For the FE simulations, balloon cross-sectional area was calculated directly from the deformed lumen contour at each output frame. The deformed nodal coordinates defining the balloon–tissue interface were ordered along the contour, and the enclosed area was calculated using the polygon-area equation:

$$A = \frac{1}{2} \left| \sum_{i=1}^{n} \left(x_i y_{i+1} - x_{i+1} y_i \right) \right|$$

Where x_i and y_i are the deformed coordinates of consecutive nodes along the balloon contour. For the quarter-symmetry model, the contour was closed along the two symmetry axes, and the calculated quarter-area was multiplied by four to obtain the equivalent full cross-sectional area.

The corresponding applied balloon pressure at each output frame was obtained from the prescribed pressure-loading history.

To provide a common measure of inflation between the experimental and simulated data, cross-sectional area was expressed relative to its initial value:

$$\Delta A_i = A_i - A_0$$

Where A_0 is the initial balloon cross-sectional area. Pressure was similarly referenced to its initial value so that both experimental and simulated responses began at (0, 0). The resulting ΔA–pressure curves therefore enabled direct comparison of cross-sectional expansion as a function of pressure between the experimental measurements and two-dimensional FE simulations.

4.3 CM stiffness sensitivity analysis

To evaluate the potential influence of CM material stiffness on the inflation response, a parametric sensitivity analysis was performed using the reference uterine geometry. Experimental indentation testing indicated an approximately twofold increase in the apparent indentation modulus of the CM following phthalate exposure [12]. Since indentation modulus cannot be directly converted to individual constitutive parameters of the GOH material model, these measurements were instead used to guide the range of stiffness changes evaluated in the simulations rather than for direct material calibration. The CM collagen fiber stiffness parameter, k_1, was therefore increased to 1.5 and 2.0 times its reference value while maintaining the reference geometry, all other material parameters, Em and LM properties, loading conditions, contact interactions, and boundary conditions unchanged. Simulated ΔA–pressure curves were generated for each case and compared with those obtained for the geometric remodeling cases.

4.4 Quantitative Comparison of Simulated Inflation Responses

To quantify differences among the simulated inflation responses, parameters were derived from the pressure–change-in-area (ΔA–P) curves over a common pressure range of 0–60 kPa. Toe- and linear-region P–ΔA slopes (kPa/mm²) were determined by linear regression of pressure as a function of cross-sectional area change:

$$P = m\Delta A + b$$

where P is the applied pressure, ΔA is the change in balloon cross-sectional area, m is the fitted P–ΔA slope, and b is the regression intercept. The toe-region slope was calculated over 0–10 kPa, whereas the linear-region slope was calculated over 30–60 kPa, with a larger slope indicating a greater pressure increase for a given increase in cross-sectional area.

The overall pressure–area response was additionally characterized by the area under the ΔA–pressure curve over the common pressure range of 0–60 kPa with AUC (mm²·kPa):

$$AUC_{\Delta A-P} = \int_0^{60\,kPa} \Delta A\, dP$$

A smaller AUC indicates less overall cross-sectional expansion over the applied pressure range and therefore greater resistance to inflation. For comparisons among the geometry and stiffness variation cases, each parameter was also expressed as the percent change relative to the reference model:

$$\%\Delta Y = \frac{Y - Y_{ref}}{Y_{ref}} \times 100$$

where Y is the ΔA–P-derived parameter for the modified model and Y_{ref} is the corresponding value for the reference model.

Data availability

The data generated and analyzed during this study are available from the corresponding author upon reasonable request.

Code availability

Custom Python scripts used for image processing, geometric quantification, and statistical analysis are available from the corresponding author upon reasonable request.

Acknowledgments

This work was supported by the National Institutes of Health (NIH) under grant numbers 5T32HD108075 and 1R35ES034988. Imaging was performed at the Carl R. Woese Institute for Genomic Biology at the University of Illinois Urbana-Champaign. Computational analyses were performed using resources provided by the Beckman Institute Visualization Laboratory at the University of Illinois Urbana-Champaign. Dr. Amy Wagoner Johnson and Dr. Indrani C. Bagchi are Biohub Investigators.

Author contributions

Conceptualization: M.R. Arshee and A. Wagoner Johnson. Methodology: M.R. Arshee, S. Caron, M.J. Laws, J.A. Flaws, I.C. Bagchi, A. Wagoner Johnson. Formal analysis: M.R. Arshee. Software: M.R. Arshee. Visualization: M.R. Arshee. Funding acquisition: J.A. Flaws, I.C. Bagchi, and A. Wagoner Johnson. Supervision: A. Wagoner Johnson. Writing- original draft: M.R. Arshee. Writing- review and editing: M.R. Arshee, I.C. Bagchi, and A. Wagoner Johnson. All authors read and approved of the final manuscript.

Competing interests

The authors declare no competing interests.

References:

1. Di Renzo, G. C., J. A. Conry, J. Blake, M. S. DeFrancesco, N. DeNicola, J. N. Martin, K. A. McCue, D. Richmond, A. Shah, P. Sutton, T. J. Woodruff, S. Z. Van Der Poel, and L. C. Giudice. International Federation of Gynecology and Obstetrics opinion on reproductive health impacts of exposure to toxic environmental chemicals. *Int. J. Gynecol. Obstet.* 131:219–225, 2015. https://doi.org/10.1016/j.ijgo.2015.09.002
2. Segal, T. R., and L. C. Giudice. Before the beginning: environmental exposures and reproductive and obstetrical outcomes. *Fertil. Steril.* 112:613–621, 2019. https://doi.org/10.1016/j.fertnstert.2019.08.001
3. Gore, A. C., V. A. Chappell, S. E. Fenton, J. A. Flaws, A. Nadal, G. S. Prins, J. Toppari, and R. T. Zoeller. EDC-2: The Endocrine Society's Second Scientific Statement on Endocrine-Disrupting Chemicals. *Endocr. Rev.* 36:E1–E150, 2015. https://doi.org/10.1210/er.2015-1010
4. Sharara, F. I., D. B. Seifer, and J. A. Flaws. Environmental toxicants and female reproduction. *Fertil. Steril.* 70:613–622, 1998. https://doi.org/10.1016/S0015-0282(98)00253-2
5. Cao, X. Phthalate Esters in Foods: Sources, Occurrence, and Analytical Methods. *Compr. Rev. Food Sci. Food Saf.* 9:21–43, 2010. https://doi.org/10.1111/j.1541-4337.2009.00093.x
6. Gao, X., B. Yang, Z. Tang, X. Luo, F. Wang, H. Xu, and X. Cai. Determination of Phthalates Released from Paper Packaging Materials by Solid-Phase Extraction–High-Performance Liquid Chromatography. *J. Chromatogr. Sci.* 52:383–389, 2014. https://doi.org/10.1093/chromsci/bmt046
7. Pagoni, A., O. S. Arvaniti, and O.-I. Kalantzi. Exposure to phthalates from personal care products: Urinary levels and predictors of exposure. *Environ. Res.* 212:113194, 2022. https://doi.org/10.1016/j.envres.2022.113194
8. Halden, R. U. Plastics and Health Risks. *Annu. Rev. Public Health* 31:179–194, 2010. https://doi.org/10.1146/annurev.publhealth.012809.103714
9. Koch, H. M., and A. M. Calafat. Human body burdens of chemicals used in plastic manufacture. *Philos. Trans. R. Soc. B Biol. Sci.* 364:2063–2078, 2009. https://doi.org/10.1098/rstb.2008.0208
10. Wang, Y., H. Zhu, and K. Kannan. A Review of Biomonitoring of Phthalate Exposures. *Toxics* 7:21, 2019. https://doi.org/10.3390/toxics7020021
11. Lee, K. J., and K. Choi. Environmental occurrence, human exposure, and endocrine disruption of di-iso-nonyl phthalate and di-iso-decyl phthalate: A systematic review. *Crit. Rev. Environ. Sci. Technol.* 54:603–640, 2024. https://doi.org/10.1080/10643389.2023.2261815
12. Shukla, R., M. R. Arshee, M. J. Laws, J. A. Flaws, M. K. Bagchi, A. J. Wagoner Johnson, and I. C. Bagchi. Chronic exposure of mice to phthalates enhances TGF beta signaling and promotes uterine fibrosis. *Reprod. Toxicol.* 122:108491, 2023. https://doi.org/10.1016/j.reprotox.2023.108491

13. Kay, V. R., C. Chambers, and W. G. Foster. Reproductive and developmental effects of phthalate diesters in females. *Crit. Rev. Toxicol.* 43:200–219, 2013. https://doi.org/10.3109/10408444.2013.766149
14. Zhang, H., D. Liu, and J. Chen. Di-2-ethylhexyl phthalate (DEHP) exposure increase female infertility. *Reprod. Toxicol.* 130:108719, 2024. https://doi.org/10.1016/j.reprotox.2024.108719
15. Parra-Forero, L. Y., I. Hernández-Ochoa, J. A. Flaws, and R. A. Nowak. Oral exposure to di(2-ethylhexyl) phthalate alters the expression of GATA6, OCT4, and CDX2 in blastocysts and decreases the rate of implantation in a mouse model. *Toxicol. Sci.* 206:68–85, 2025. https://doi.org/10.1093/toxsci/kfaf057
16. Li, R., C. Yu, R. Gao, X. Liu, J. Lu, L. Zhao, X. Chen, Y. Ding, Y. Wang, and J. He. Effects of DEHP on endometrial receptivity and embryo implantation in pregnant mice. *J. Hazard. Mater.* 241–242:231–240, 2012. https://doi.org/10.1016/j.jhazmat.2012.09.038
17. Toft, G., B. A. G. Jönsson, C. H. Lindh, T. K. Jensen, N. H. Hjollund, A. Vested, and J. P. Bonde. Association between Pregnancy Loss and Urinary Phthalate Levels around the Time of Conception. *Environ. Health Perspect.* 120:458–463, 2012. https://doi.org/10.1289/ehp.1103552
18. Laws, M. J., D. D. Meling, A. R. K. Deviney, R. Santacruz-Márquez, and J. A. Flaws. Long-term exposure to di(2-ethylhexyl) phthalate, diisononyl phthalate, and a mixture of phthalates alters estrous cyclicity and/or impairs gestational index and birth rate in mice. *Toxicol. Sci.* 193:48–61, 2023. https://doi.org/10.1093/toxsci/kfad030
19. Richardson, K. A., P. R. Hannon, Y. J. Johnson-Walker, M. S. Myint, J. A. Flaws, and R. A. Nowak. Di (2-ethylhexyl) phthalate (DEHP) alters proliferation and uterine gland numbers in the uteri of adult exposed mice. *Reprod. Toxicol.* 77:70–79, 2018. https://doi.org/10.1016/j.reprotox.2018.01.006
20. Shanmugam, D. A. S., S. Dhatchanamurthy, K. A. Leela, and R. S. Bhaskaran. Maternal exposure to di(2-ethylhexyl) phthalate (DEHP) causes multigenerational adverse effects on the uterus of F1 and F2 offspring rats. *Reprod. Toxicol.* 115:17–28, 2023. https://doi.org/10.1016/j.reprotox.2022.11.006
21. Myers, K. M., and D. Elad. Biomechanics of the human uterus. *WIREs Syst. Biol. Med.* 9:e1388, 2017. https://doi.org/10.1002/wsbm.1388
22. Jorge, S., S. Chang, J. J. Barzilai, P. Leppert, and J. H. Segars. Mechanical Signaling in Reproductive Tissues: Mechanisms and Importance. *Reprod. Sci.* 21:1093–1107, 2014. https://doi.org/10.1177/1933719114542023
23. Leftwich, M. C., and A. C. Baumer. The Fluid Mechanics of Female Reproduction: A Review of the Biofluid Mechanics of Pregnancy and Delivery. *Annu. Rev. Fluid Mech.* 56:171–188, 2024. https://doi.org/10.1146/annurev-fluid-121021-033738
24. Kagami, K., M. Ono, T. Iizuka, T. Matsumoto, T. Hosono, N. Sekizuka-Kagami, Y. Shinmyo, H. Kawasaki, and H. Fujiwara. A novel third mesh-like myometrial layer connects the longitudinal and circular muscle fibers -A potential stratum to coordinate uterine contractions-. *Sci. Rep.* 10:8274, 2020. https://doi.org/10.1038/s41598-020-65299-0
25. Fodera, D. M., E. Z. Xu, C. A. Duarte, M. H. Wyss, S. Fang, X. Chen, M. L. Oyen, J. Vink, I. Rosado-Mendez, H. Feltovich, T. J. Hall, and K. M. Myers. Time-dependent material

properties and composition of the nonhuman primate uterine layers through gestation. *Sci. Rep.* 15:23194, 2025. https://doi.org/10.1038/s41598-025-02986-w
26. Moghaddam, A. O., J. Wei, J. Kim, A. C. Dunn, and A. J. Wagoner Johnson. An indentation-based approach to determine the elastic constants of soft anisotropic tissues. *J. Mech. Behav. Biomed. Mater.* 103:103539, 2020. https://doi.org/10.1016/j.jmbbm.2019.103539
27. Moghaddam, A. O., Z. Lin, M. Sivaguru, H. Phillips, B. L. McFarlin, K. C. Toussaint, and A. J. W. Johnson. Heterogeneous microstructural changes of the cervix influence cervical funneling. *Acta Biomater.* 140:434–445, 2022. https://doi.org/10.1016/j.actbio.2021.12.025
28. Ostadi Moghaddam, A., M. R. Arshee, Z. Lin, M. Sivaguru, H. Phillips, B. L. McFarlin, K. C. Toussaint, and A. J. Wagoner Johnson. Orientation-dependent indentation reveals the crosslink-mediated deformation mechanisms of collagen fibrils. *Acta Biomater.* 158:347–357, 2023. https://doi.org/10.1016/j.actbio.2023.01.005
29. Tang, V. W. Collagen, stiffness, and adhesion: the evolutionary basis of vertebrate mechanobiology. *Mol. Biol. Cell* 31:1823–1834, 2020. https://doi.org/10.1091/mbc.E19-12-0709
30. Shukla, R., A. Mahmuda, M. J. Laws, J. A. Flaws, M. K. Bagchi, A. J. Wagoner Johnson, and I. C. Bagchi. Chronic exposure of mice to phthalates enhances TGF beta signaling and promotes uterine fibrosis. Physiology, 2023. https://doi.org/10.1101/2023.05.10.540240
31. Andrus, A. R., L. Y. Parra-Forero, C. N. Sexton, K. C. Liu, S. M. Rush, M. J. Laws, J. A. Flaws, and R. A. Nowak. Acute exposure to di(2-ethylhexyl) phthalate or diisononyl phthalate leads to increased inflammation and oxidative stress in the uteri of mice. *Reprod. Toxicol.* 144:109306, 2026. https://doi.org/10.1016/j.reprotox.2026.109306
32. Li, K., M. Liszka, C. Zhou, E. Brehm, J. A. Flaws, and R. A. Nowak. Prenatal exposure to a phthalate mixture leads to multigenerational and transgenerational effects on uterine morphology and function in mice. *Reprod. Toxicol.* 93:178–190, 2020. https://doi.org/10.1016/j.reprotox.2020.02.012
33. Shukla, R., A. Kannan, M. J. Laws, A. Wagoner Johnson, J. A. Flaws, M. K. Bagchi, and I. C. Bagchi. Exposure to phthalates enhances estrogen and beta-catenin signaling pathways, leading to endometrial hyperplasia in mice. *Toxicol. Sci.* 206:58–67, 2025. https://doi.org/10.1093/toxsci/kfaf062
34. Moseley, T., A. J. Hicks, E. M. Cosgriff-Hernandez, M. K. Rausch, and J. Hakim. Finite element modeling in obstetrics and gynecology: advances, applications, and challenges. *Front. Med.* 12:1606989, 2025. https://doi.org/10.3389/fmed.2025.1606989
35. Westervelt, A. R., M. Fernandez, M. House, J. Vink, C.-L. Nhan-Chang, R. Wapner, and K. M. Myers. A Parameterized Ultrasound-Based Finite Element Analysis of the Mechanical Environment of Pregnancy. *J. Biomech. Eng.* 139:051004, 2017. https://doi.org/10.1115/1.4036259
36. Yue, H., Y. Tian, X. Wu, X. Yang, P. Xu, H. Zhu, and N. Sang. Exploration of the damage and mechanisms of BPS exposure on the uterus and ovary of adult female mice. *Sci. Total Environ.* 868:161660, 2023. https://doi.org/10.1016/j.scitotenv.2023.161660

37. Kendziorski, J. A., and S. M. Belcher. Effects of whole life exposure to Bisphenol A or 17α-ethinyl estradiol in uterus of nulligravida CD1 mice. *Data Brief* 5:948–953, 2015. https://doi.org/10.1016/j.dib.2015.10.034
38. Diantini, N. S. E., S. Soeharto, and I. W. A. Wiyasa. The effect of lead acetate administration to the uterine malondialdehyde level and endometrial thickness in albino rats (Rattus novergicus). *Med. J. Indones.* 27:150–4, 2018. https://doi.org/10.13181/mji.v27i3.2031
39. Gordts, S., G. Grimbizis, V. Tanos, P. Koninckx, and R. Campo. Junctional zone thickening: an endo-myometrial unit disorder. *Facts Views Vis. ObGyn* 15:309–316, 2023. https://doi.org/10.52054/FVVO.15.4.109
40. Nasiadek, M., M. Danilewicz, M. Klimczak, J. Stragierowicz, and A. Kilanowicz. Subchronic Exposure to Cadmium Causes Persistent Changes in the Reproductive System in Female Wistar Rats. *Oxid. Med. Cell. Longev.* 2019:1–17, 2019. https://doi.org/10.1155/2019/6490820
41. Wang, H., and S. K. Dey. Roadmap to embryo implantation: clues from mouse models. *Nat. Rev. Genet.* 7:185–199, 2006. https://doi.org/10.1038/nrg1808
42. Ramathal, C., I. Bagchi, R. Taylor, and M. Bagchi. Endometrial Decidualization: Of Mice and Men. *Semin. Reprod. Med.* 28:017–026, 2010. https://doi.org/10.1055/s-0029-1242989
43. Li, Q., A. Kannan, F. J. DeMayo, J. P. Lydon, P. S. Cooke, H. Yamagishi, D. Srivastava, M. K. Bagchi, and I. C. Bagchi. The Antiproliferative Action of Progesterone in Uterine Epithelium Is Mediated by Hand2. *Science* 331:912–916, 2011. https://doi.org/10.1126/science.1197454
44. Cha, J., X. Sun, and S. K. Dey. Mechanisms of implantation: strategies for successful pregnancy. *Nat. Med.* 18:1754–1767, 2012. https://doi.org/10.1038/nm.3012
45. Wu, X., K. G. Morgan, C. J. Jones, R. M. Tribe, and M. J. Taggart. Myometrial mechanoadaptation during pregnancy: implications for smooth muscle plasticity and remodelling. *J. Cell. Mol. Med.* 12:1360–1373, 2008. https://doi.org/10.1111/j.1582-4934.2008.00306.x
46. Oldenhof, A. D., O. P. Shynlova, M. Liu, B. L. Langille, and S. J. Lye. Mitogen-activated protein kinases mediate stretch-induced c- *fos* mRNA expression in myometrial smooth muscle cells. *Am. J. Physiol.-Cell Physiol.* 283:C1530–C1539, 2002. https://doi.org/10.1152/ajpcell.00607.2001
47. Dalrymple, A., K. Mahn, L. Poston, E. Songu-Mize, and R. M. Tribe. Mechanical stretch regulates TRPC expression and calcium entry in human myometrial smooth muscle cells. *MHR Basic Sci. Reprod. Med.* 13:171-179*, 2007. https://doi.org/10.1093/molehr/gal110
48. Loudon, J. A. Z., S. R. Sooranna, P. R. Bennett, and M. R. Johnson. Mechanical stretch of human uterine smooth muscle cells increases IL-8 mRNA expression and peptide synthesis. *MHR Basic Sci. Reprod. Med.* 10:895–899, 2004. https://doi.org/10.1093/molehr/gah112
49. Terzidou, V., S. R. Sooranna, L. U. Kim, S. Thornton, P. R. Bennett, and M. R. Johnson. Mechanical Stretch Up-Regulates the Human Oxytocin Receptor in Primary Human

Uterine Myocytes. *J. Clin. Endocrinol. Metab.* 90:237–246, 2005. https://doi.org/10.1210/jc.2004-0277
50. Li, Y., M. Reznichenko, R. M. Tribe, P. E. Hess, M. Taggart, H. Kim, J. P. DeGnore, S. Gangopadhyay, and K. G. Morgan. Stretch Activates Human Myometrium via ERK, Caldesmon and Focal Adhesion Signaling. *PLoS ONE* 4:e7489, 2009. https://doi.org/10.1371/journal.pone.0007489
51. Arshee, M., C. M. Luetkemeyer, I. C. Bagchi, A. Ziv-Gal, J. Flaws, A. Safar, and A. Wagoner Johnson. Image-Informed Inverse Finite Element Analysis Reveals Altered Constitutive Behavior Following Controlled Uterine Tissue Remodeling. 2026. https://doi.org/10.64898/2026.08.23.746519
52. Domingo, M. J. E., T. N. Vanoven, R. De Vita, M. E. F. Rodriguez, K. S. Miller, and I. J. Pence. Biomechanical and Compositional Changes in the Murine Uterus with Age. *Ann. Biomed. Eng.* 53:1385–1398, 2025. https://doi.org/10.1007/s10439-025-03709-y
53. Robison, K. M., C. K. Conway, L. Desrosiers, L. R. Knoepp, and K. S. Miller. Biaxial Mechanical Assessment of the Murine Vaginal Wall Using Extension–Inflation Testing. *J. Biomech. Eng.* 139:104504, 2017. https://doi.org/10.1115/1.4037559
54. Gasser, T. C., R. W. Ogden, and G. A. Holzapfel. Hyperelastic modelling of arterial layers with distributed collagen fibre orientations. *J. R. Soc. Interface* 3:15–35, 2006. https://doi.org/10.1098/rsif.2005.0073
55. Chen, X., O. Nadiarynkh, S. Plotnikov, and P. J. Campagnola. Second harmonic generation microscopy for quantitative analysis of collagen fibrillar structure. *Nat. Protoc.* 7:654–669, 2012. https://doi.org/10.1038/nprot.2012.009
56. Abraham, T., G. Fong, and A. Scott. Second harmonic generation analysis of early Achilles tendinosis in response to in vivo mechanical loading. *BMC Musculoskelet. Disord.* 12:26, 2011. https://doi.org/10.1186/1471-2474-12-26

Supplementary Files

This is a list of supplementary files associated with this preprint. Click to download.

- SupplementaryDocumentphthalatepaper.docx